AIAA JOURNAL
Vol. 48, No. 7, July 2010

Effect of Velocity Ratio on Noise Source Distribution of Coaxial Jets

Dimitri Papamoschou* and Sara Rostamimonjezi†
University of California, Irvine, Irvine, California 92697-3975

DOI: 10.2514/1.J050140

The noise source distribution of coaxial jets with a diameter ratio of 1.6 and variable velocity ratio is investigated with a small-aperture microphone phased array. The array design enables differentiation of noise emitted by large-scale and fine-scale turbulence structures, which have different directivities. The acoustic data are complemented by pitot surveys of the mean flow, which yield measurements of the primary and secondary cores of the jet. For zero velocity ratio (single-stream jet), the region near the nozzle emits strong high-frequency noise. Increasing the secondary-to-primary velocity ratio suppresses the near-nozzle noise and extends the location of the peak noise downstream, which increases moderately. The axial location of peak noise is approximately situated at the end of the primary core. The suppression of high-frequency noise is explained by the creation and elongation of the secondary core as the velocity ratio increases. The acoustic trends with velocity ratio are similar for small and large array observation angles from which large-scale and fine-scale turbulence noise, respectively, have been shown to radiate. However, the increase in peak noise is more pronounced for the large-scale noise.

Nomenclature

D	=	nozzle diameter
F	=	static thrust
f	=	cyclic frequency
G_{mn}	=	cross-spectrum matrix
$\ell_m(x)$	=	distance of microphone m from focus point x
M	=	jet exit Mach number
m_0	=	number of microphones
R	=	array radius
Sr	=	Strouhal number, fD_p/U_p
$s(x,t)$	=	delay-and-sum array output
t	=	time
U	=	jet exit velocity
u	=	jet mean velocity
w_m	=	weight for microphone m
$\bar{w}_m$	=	dimensionless weight for microphone m
x, y, z	=	spatial coordinates
ϵ_m	=	weighted steering vector
θ	=	polar angle from jet axis
λ	=	wavelength
$\Phi(x,\omega)$	=	array power spectrum, $\mathrm{Pa}^2/\mathrm{Hz}$
$\Phi_{\mathrm{SPL}}(x,f)$	=	lossless array sound pressure level spectrum, dB/Hz
τ_m	=	time delay for microphone m
ω	=	radian frequency, $2\pi f$

Subscripts

a	=	average among microphones
p	=	primary
s	=	secondary
wa	=	weighted average among microphones

Received 17 August 2009; revision received 18 February 2010; accepted for publication 23 February 2010.

*Professor, Department of Mechanical and Aerospace Engineering; dpapamos@uci.edu. Fellow AIAA.

†Graduate Researcher, Department of Mechanical and Aerospace Engineering; srostami@uci.edu.

I. Introduction

NOISE from coaxial jets is of great relevance to aeroacoustics because the majority of civilian turbofan engines have a coaxial exhaust. Early works on coaxial jets were motivated mainly by applications in combustion and aircraft propulsion. Forstall and Shapiro [1] conducted an experimental investigation on mass and momentum transfer between the two streams of a coflowing jet with very large secondary flows. They determined that the velocity ratio of the primary to secondary stream is the principal variable determining the shape of the mixing region. An empirical relation for the length of the primary potential core was proposed. Other works in subsonic, axisymmetric, turbulent coaxial jets have studied the near-field region at various velocity ratios. Ko and Kwan [2], Champagne and Wygnanski [3], and Durao and Whitelaw [4] investigated the development of the flowfield and its approach to a self-preserving state. These studies concluded that the instability and flow development depend on the velocity and density ratios across the shear layers. Williams et al. [5] investigated the flow structure and acoustics of cold subsonic coaxial jets and suggested a method of predicting the noise attenuation when the jet is surrounded by an annular flow of variable velocity. Murakami and Papamoschou [6] conducted a parametric study of the mean flowfield of coaxial jets and noted the substantial elongation of the primary potential core with addition of a secondary flow. Bogey et al. [7] carried out numerical simulations of hot coaxial jets and noted that the noise generation is significant near the end of the two potential cores.

A number of studies have investigated the acoustic differences between a coaxial jet and a single jet [8–10]. Tanna [8] concluded that subsonic coaxial jets with normal velocity profile are noisier, in terms of overall sound pressure level, when compared to a single equivalent jet (SEJ) with the same thrust, mass flow rate, and exit area. Although Tanna's SEJ is generally quieter than the coaxial jet, the comparison basis may not be realistic from a thermodynamic point of view because the total enthalpy is not conserved. Zaman and Dahl [10] used the criterion of equal enthalpy, instead of equal area, to define the SEJ and basically arrived at the same conclusions as Tanna [8]. On the other hand, experiments on supersonic coaxial jets by Papamoschou [11] showed that the coaxial jet is slightly quieter than the enthalpy-based SEJ. It therefore appears that the acoustic differences between a coaxial jet and its SEJ depend on the flow parameters. For jets representing modern high-bypass engines, there is little doubt that the SEJ is quieter than the coaxial jet. However, the uniformly mixed SEJ is an idealization. In practice, the exhaust is nonuniform and the mixer can inflict significant installation, weight, and drag penalties. For these and other practical considerations the majority of high-bypass engines are of the unmixed (separate-flow) type. This is the reason coaxial jets remain the focus of intense

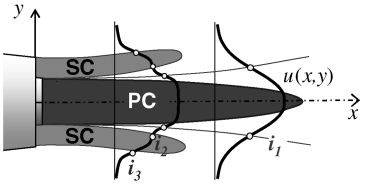

Fig. 1 Basic elements of mean flow in a coaxial jet.

activity to understand their fluid dynamics and acoustics, and to suppress their noise.

The present work is motivated by the ability of the secondary flow in a coaxial jet to suppress noise from the primary flow. Fisher et al. [12] studied coaxial jets with normal velocity profile and suggested that in the initial region, the primary shear layer makes negligible contribution to sound emission. Papamoschou [13] extended this concept to a secondary core defined by the inflection points of the velocity profile and showed that the convective Mach number of eddies in the initial region has very low value. We briefly review here the essential elements of Papamoschou's mean flow model, as shown in Fig. 1. The primary core (PC) is defined as the region where the velocity exceeds a high threshold, typically 80 to 90% of the core exit velocity, and thus represents the region of the most intense noise sources. The secondary core (SC) is defined by the outer inflection points i_2 and i_3 of the radial velocity profile, which form a loop. The ability of the secondary core to silence the primary shear layer is the foundation of noise-reduction concepts that extend the secondary core (via offset nozzles or deflectors) to cover a greater portion of the primary shear layer that emits downward noise [11,13–17].

The advent of noise source location techniques, such as microphone phased arrays [18–24] provides an opportunity for a more detailed investigation of the noise sources in coaxial jets and their dependence on velocity ratio. By covering a large range of the velocity ratio we hope to get a bigger picture of the noise source characteristics, and differences from the single jet, than possible through studies at fixed conditions. Of particular interest are the silencing of the initial region and the downstream extension of noise sources due to the elongation of the primary potential core. The phased array measurements are combined with mean velocity surveys to assess the connections between mean flow and noise source distribution. The experiments are conducted using cold air jets, so they do not capture potential effects of temperature on the noise source. It should be noted, however, that analysis of hot-jet data by Bridges [25] has shown that the effect of temperature on turbulence statistics is weak once changes in the potential core length have been accounted for.

II. Experimental Setup

A. Flow Facility

Experiments were conducted in the University of California, Irvine's Jet Aeroacoustics Facility, described in earlier publications [26]. A coaxial dual-stream nozzle with exit diameters $D_p = 14.2$ mm and $D_s = 23.4$ mm was employed. The lip thickness of the inner nozzle was 0.76 mm, resulting in an effective (area-based) diameter of the combined nozzle $D_{\text{eff}} = 22.4$ mm. The nozzle coordinates are plotted in Fig. 2. Air at room temperature was supplied to the primary and secondary streams. The Mach number of the primary stream was fixed at $M_p = 0.9$ and the secondary Mach number M_s was varied from 0 to 0.9. Table 1 lists the flow conditions. Cases are labeled according to their velocity ratio (i.e., *R*036 means $U_s/U_p = 0.356$). The Reynolds number of the primary jet was 3.6×10^5. For the coaxial jet, for $U_s/U_p = 1$, the Reynolds number based on the secondary diameter D_s was 5.9×10^5. Static thrust was estimated from the calculated flow conditions at the nozzle exit. Only the cases with secondary Mach number M_s from 0 to 0.9 in increments of 0.15 were investigated in the acoustics tests. The sound pressure level spectra from the primary jet, issued from the specific nozzle of this study, have been shown to compare very well with spectra for similar jets in larger-scale facilities [10].

Table 1 Flow conditions ($M_p = 0.90, U_p = 285$ m/s)

Case	M_s	U_s, m/s	U_s/U_p	$F(N)$
*R*000	0.000	0.0	0.000	18.5
*R*018	0.150	51.0	0.179	19.1
*R*036	0.300	101.0	0.356	21.6
*R*053	0.450	151.0	0.528	25.4
*R*069	0.600	198.0	0.694	31.0
*R*077	0.675	220.6	0.774	33.5
*R*085	0.750	243.0	0.852	37.7
*R*093	0.825	264.2	0.927	40.1
*R*100	0.900	285.0	1.000	46.1

Noise measurements were conducted inside an anechoic chamber using a microphone array comprising eight 3.2 mm condenser microphones (Brüel & Kjaer model 4138) arranged on a circular arc centered at the vicinity of the nozzle exit. Figure 3 shows the acoustic setup. The polar aperture of the array for this experiment was 30° and the array radius was 1 m. The angular spacing of the microphones was logarithmic, starting from 2° for microphones 1 and 2 and ending with 10° for microphones 7 and 8. Uneven microphone spacing was used to mitigate the effects of spatial aliasing. The entire array

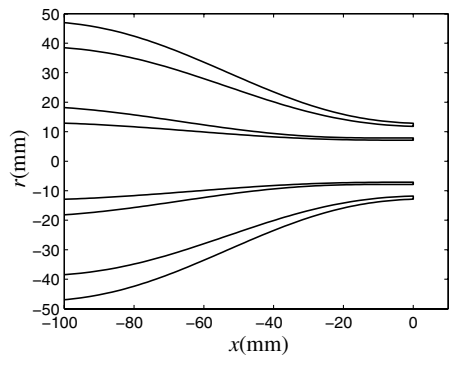

Fig. 2 Nozzle coordinates.

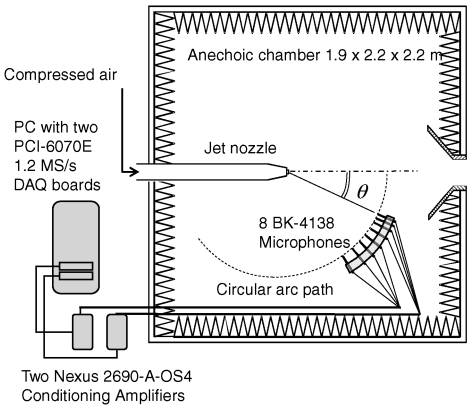

Fig. 3 Microphone array setup.

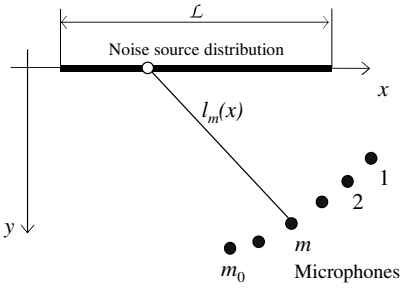

Fig. 4 Linear distribution of noise sources and microphone array.

Table 2 Microphone array parameters

$\theta_{wa} = 30°$		$\theta_{wa} = 99°$	
θ	$\bar{w}$	θ	$\bar{w}$
17.1	1.00	76.8	0.56
19.0	1.00	78.6	0.67
21.3	1.00	80.8	0.80
23.9	1.00	83.3	0.92
27.1	1.00	86.4	1.00
31.3	1.00	90.4	0.95
37.0	1.00	95.0	0.57
45.8	1.00	105.5	0.17

structure was rotated around its center to place the array at the desired observation angle. The distances between the centers of the microphone grids were measured with accuracy of 0.1 mm using a digital caliper. A geometric calibration procedure provided the position of each microphone relative to the nozzle exit with accuracy of 2 mm. The microphones were connected, in groups of four, to two amplifier/signal conditioners (Brüel & Kjaer Nexus 2690-A-OS4) with low-pass filter set at 100 kHz and high-pass filter set at 300 Hz. The four-channel output of each amplifier was sampled at 250 kHz per channel by a multifunction data acquisition board (National Instruments PCI-6070E). Two such boards, one for each amplifier, were installed in a Pentium 4 personal computer. National Instruments LabVIEW software was used to acquire the signals. For each jet configuration the array was placed at four positions, the polar angle of the first microphone taking the values 15, 40, 65, and 90 deg. The sound pressure level spectrum was corrected for actuator response, free-field correction, and atmospheric absorption. The overall sound pressure level (OASPL) was obtained by integrating the corrected spectrum. Spectra and OASPL are referenced to a radius of 100 D_p from the nozzle exit. Based on the repeatability of acoustic measurement for the primary jet of this study under different humidity and temperature conditions, the uncertainty in OASPL is estimated at 0.3 dB.

B. Beam Forming

The modeling of the jet noise source follows the traditional method, used in past beamforming studies [18,20,21] of treating the jet as a line of spatially uncorrelated monopoles (Fig. 4). This is a simplified approach of detecting an equivalent noise source distribution that radiates to the far field. The narrow aperture of the present array allows discrimination of noise sources radiating at small and large angles to the jet axis, corresponding to large-scale and fine-scale noise, respectively, as proposed by Tam [27]. Detailed near-field pressure measurements by Tinney and Jordan [28] provide evidence of these two distinct noise sources in coaxial jets as well.

In this section we present only a brief overview of the noise source location technique for the narrow-aperture array. Further details, including assessment of the spatial resolution, can be found in Papamoschou and Dadvar [22]. Referring to Fig. 4, beamforming uses the traditional delay-and-sum method:

$$s(t) = \sum_{m=1}^{m_0} w_m p_m(t + \tau_m) \tag{1}$$

where $p_m(t)$ is the pressure fluctuation measured by microphone m, w_m are weights, and

$$\tau_m = \frac{\ell_m(x)}{a} \tag{2}$$

is the time delay for sound to propagate from the steering point x to microphone m. The power spectrum of $s(t)$ is

$$\Phi(x,\omega) = \sum_{m=1}^{m_0}\sum_{n=1}^{m_0} w_m w_n e^{i\omega(\tau_m-\tau_n)}\langle P_m(\omega)P_n^*(\omega)\rangle \tag{3}$$

where

$$P_m(\omega) = \int_{-\infty}^{\infty} p_m(t)e^{-i\omega t}\,\mathrm{d}t \tag{4}$$

Defining the cross-spectrum matrix as

$$G_{mn} \equiv \langle P_m(\omega)P_n^*(\omega)\rangle \tag{5}$$

we have

$$\Phi(x,\omega) = \sum_{m=1}^{m_0}\sum_{n=1}^{m_0} w_m w_n e^{i\omega(\tau_m-\tau_n)}G_{mn} \tag{6}$$

or

$$\Phi(x,\omega) = \epsilon\mathbf{G}\epsilon^T \tag{7}$$

where

$$\epsilon_m(x,\omega) = w_m(x,\omega)e^{i\omega\tau_m(x)} \tag{8}$$

is the weighted steering vector and superscript T denotes its complex transpose. Equation (7) formed the basis for the computation of the array power spectrum from the microphone pressure traces.

It is important to realize that the array output given by Eq. (7) is a convolution between the source distribution (assumed incoherent) and the point spread function. A primary consideration in selecting the form of the weights is that the area under the main lobe of the point spread function remain substantially constant with variable x. This prevents artificial distortions of the apparent source distribution due to axial variation of the point spread function. Earlier research [22] has shown that this is achievable by making the weights inversely proportional to the transverse distance of the microphone from the line source, $w_m \sim 1/y_m$. To maintain constant beam width with frequency, the weights include the frequency dependence $w_m \sim \sqrt{Sr}$. The resulting form for the weights is

$$w_m = \frac{R}{\sum_1^{m_0}\bar{w}_m}\bar{w}_m\frac{y_m}{y_a}\sqrt{Sr} \tag{9}$$

The nondimensional weights $\bar{w}_m$ were selected so that the beam width in the middle of the region of interest (around $x/D_p = 10$) was approximately equal for the two array positions shown in Fig. 5. Table 2 provides the microphone angles and nondimensional weights for each array position. The array observation polar angle is defined as the weighted average of the microphone polar angles:

$$\theta_{wa} = \frac{\sum_1^{m_0} w_m\theta_m}{\sum_1^{m_0} w_m} \tag{10}$$

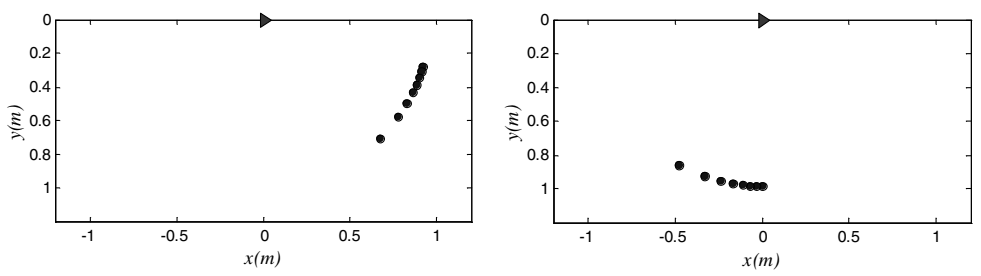

Fig. 5 Array positions used for beamforming: a) $\theta_{wa} = 30°$ and b) $\theta_{wa} = 99°$; triangles indicate nozzle exit.

Computation of the cross-spectrum matrix, Eq. (5), involved the following steps. Each microphone signal consisted of $N_s = 2^{18} = 262,144$ samples acquired at a sampling rate $F_s = 250$ kHz. The maximum resolvable (Nyquist) frequency was $F_s/2 = 125$ kHz, although the low-pass filter was set a little lower at $f = 100$ kHz. The size of the fast Fourier transform was $N_{\text{FFT}} = 2048$ yielding a frequency resolution of 122 Hz. Each signal was divided into $K = 64$ blocks of 4096 samples each, and the data within each block were windowed using a Hamming window. The cross-spectrum matrix G^k_{mn} for block k was computed using Fortran routines for autospectra and cross-spectra. The total cross-spectrum matrix was obtained from

$$G_{mn}(f) = \frac{1}{KW_h}\sum_{k=1}^{K} G^k_{mn}(f) \tag{11}$$

where W_h is a weighting constant for the Hamming window.

To present the array power spectrum in the form of lossless sound pressure level spectrum (units of dB/Hz), the following procedure was used:

$$\Phi_{\text{SPL}}(x,f) = 10\log_{10}[\Phi(x,f)] + 93.98 - C_{\text{fr}}(f) - C_{\text{ff}}(f) + \alpha(f)\ell_a(x) \tag{12}$$

The constant 93.98 comes from the normalization of the pressure by the reference pressure of 20 μPa, that is, $-20\log_{10}(20\times10^{-6}) = 93.98$. C_{fr} and C_{ff} are the corrections for the actuator response and free-field response, respectively; they are based on data provided by the manufacturer of the microphone and are practically the same for all the microphones. α is the atmospheric absorption coefficient (dB/m), computed using the formulas proposed by Bass et al. [29] for the measured values of relative humidity and temperature of the ambient air. The absorption correction is based on the average distance $\ell_a(x)$ of the microphones from the focus point. The last step in the processing involves smoothing of the array power spectrum in frequency, using a Savitzky–Golay filter [30], to remove spurious wiggles that are unrelated to jet noise physics.

The beamforming results are presented for two array observation angles, as defined by Eq. (10): $\theta_{\text{wa}} = 30$ and 99°. They correspond to noise generated by large-scale and fine-scale turbulence, respectively [27]. The placement of the microphones for each observation angle is plotted in Fig. 5.

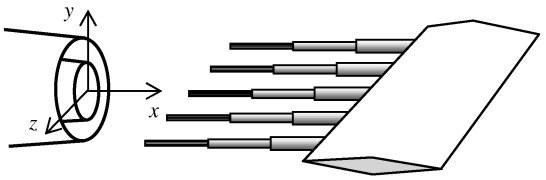

Fig. 6 Setup of pitot rake.

C. Mean Flow Surveys

The mean axial velocity in the jet plume was surveyed using a pitot rake system consisting of five probes, spaced apart by 10 mm, with hypodermic 0.5-mm-i.d. tips, as shown in Fig. 6. The very small diameter of the probe tips allowed a fine resolution of the velocity data, which facilitated the study of the inflectional layers in the jet plume. Each probe was connected individually to a Setra model 207 pressure transducer. Mounted on a motorized stage, the rake traversed the plume at constant speed in the y direction with the center probe on the $z = 0$ plane. Forty-two axial stations were surveyed, the first 28 spaced apart by 6.35 mm and the last 14 spaced apart by 12.7 mm. The total axial span surveyed was 342.9 mm or 24 inner jet diameters. Even though these were essentially 2-D surveys based on the readings of the center probe, the readings of the surrounding probes were important in ascertaining symmetry so that the center probe was indeed on the $z = 0$ plane. The speed of the y travel, 5 mm/s, was selected carefully after evaluating the time response of the pitot rake system by traversing at different speeds and ensuring that the details of the velocity profile matched those measured when traversing at very low speed.

Mach number and velocity fields were computed from the pitot measurements under the assumptions of constant static pressure equal to the ambient pressure and constant total temperature equal to the room temperature. Based on the accuracy of transducers, as provided by the manufacturer and verified by our own calibration, the pitot pressures were measured with accuracy of 0.45 kPa. The resulting error in the velocity measurement was 3.23, 0.66, and 0.23% for velocity magnitudes of 100, 200, and 285 m/s, respectively. Smoothing of the velocity profiles and computation of the second derivative was performed using a Savitzky–Golay filter [30]. The filter size was variable with very small size near the nozzle exit and larger size at far downstream distances. In the vicinity of the nozzle, where resolution of the inflectional layers was critical, the filter size was typically 2% of the inner jet diameter.

III. Results

A. Acoustics

The far-field acoustics are examined first. Figure 7 plots the directivity of the OASPL for different velocity ratios. It is important to realize that as the velocity ratio rises, the thrust of the jet increases. The OASPL data, and the spectra shown later, are not adjusted for constant thrust. With increasing U_s/U_p, the OASPL first decreases then increases. The minimum OASPL occurs at $U_s/U_p = 0.53$. For $U_s/U_p = 1.0$, where the jet becomes essentially a single jet issuing from a larger nozzle diameter, the OASPL is uniformly 4 dB above the OASPL of the single jet. This matches the increase one would predict from geometric thrust scaling arguments:

$$\Delta\text{OASPL} = 10\log_{10}\left(\frac{F_{R100}}{F_{R000}}\right) = 10\log_{10}\left(\frac{D^2_{\text{eff}}}{D^2_p}\right) = 3.9 \text{ dB}$$

The lossless narrowband SPL spectra in the direction of peak emission ($20° < \theta < 30°$, depending on velocity ratio) are plotted in

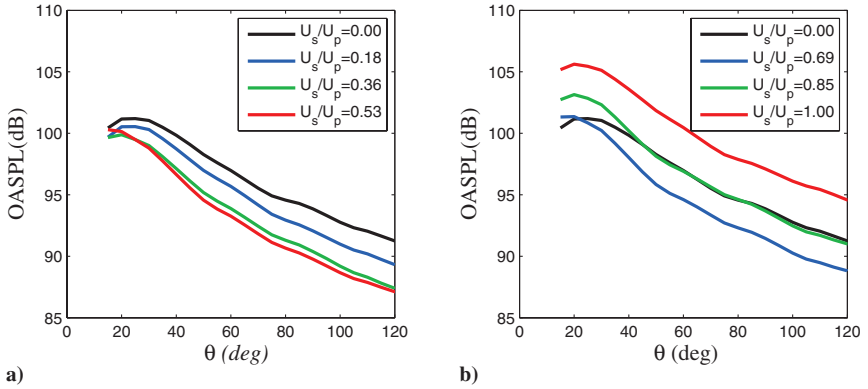

Fig. 7 Overall sound pressure level versus polar angle: a) $U_s/U_p < 0.69$ and b) $U_s/U_p \geq 0.69$.

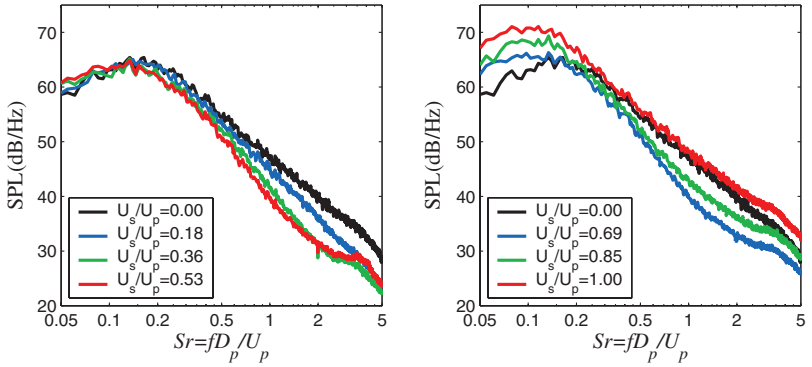

Fig. 8 Spectra in the direction of peak emission: a) $U_s/U_p < 0.69$ and b) $U_s/U_p \geq 0.69$.

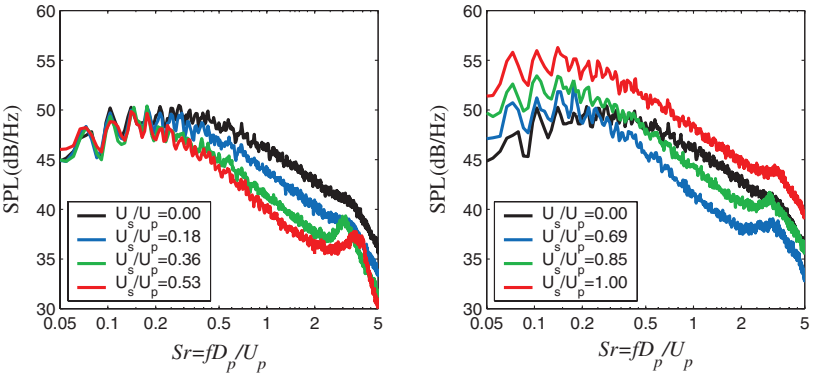

Fig. 9 Spectra in the 90 deg direction: a) $U_s/U_p < 0.69$ and b) $U_s/U_p \geq 0.69$.

Fig. 8. The overall trend with velocity ratio is the same as with the OASPL, i.e., a decrease followed by an increase in spectral levels as U_s/U_p increases from zero. For $0 < U_s/U_p \leq 0.53$, the spectrum decreases for Strouhal numbers greater than the peak value of $S_r \approx 0.15$, while the low-frequency end of the spectrum stays practically unchanged. Increasing the velocity ratio above $U_s/U_p = 0.53$ increases the high-frequency part of the spectrum (relative to the minimum value attained at $U_s/U_p = 0.53$) as well as the

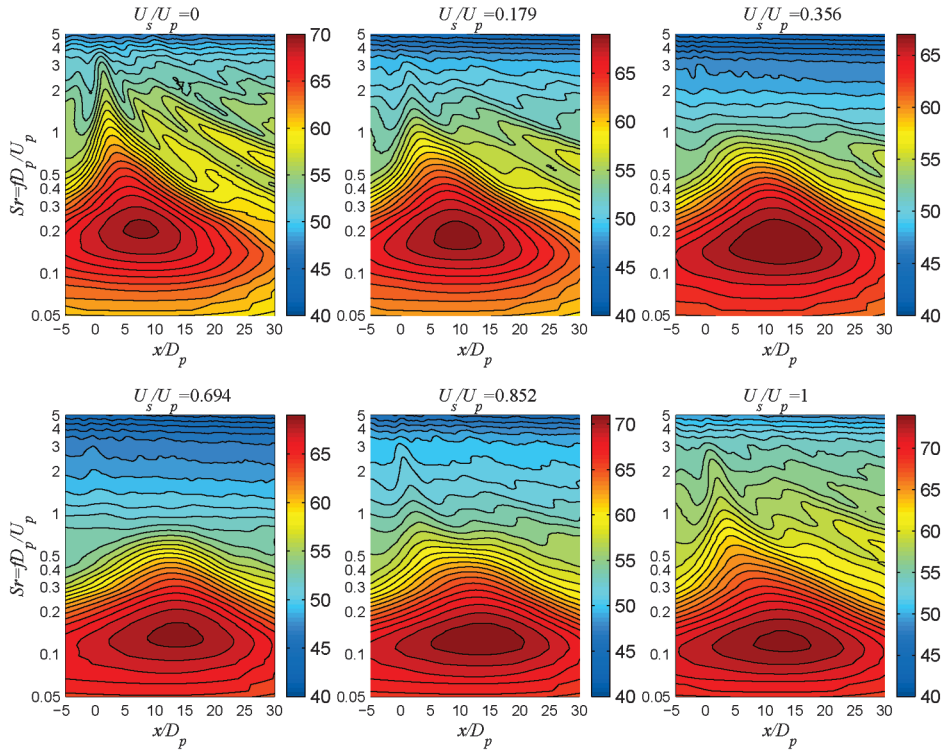

Fig. 10 Isocontours of Φ_{SPL} in the direction $\theta_{\mathrm{wa}} = 30°$ and for various velocity ratios.

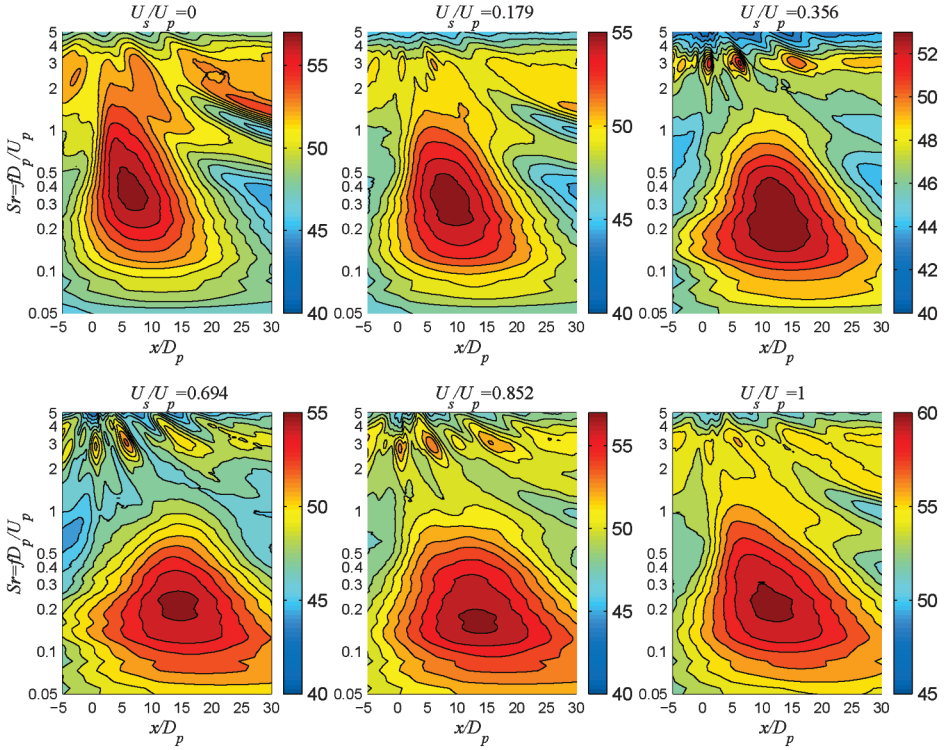

Fig. 11 Isocontours of Φ_{SPL} in the direction $\theta_{\mathrm{wa}} = 99°$ and for various velocity ratios.

low-frequency end (relative to the single jet). For $U_s/U_p = 1$, the entire spectrum is above that of the single jet. Had the $U_s/U_p = 1$ spectrum been plotted against the Strouhal number based D_{eff}, it would have been uniformly higher than the spectrum for $U_s/U_p = 0$ by about 4 dB. The trends observed for the spectra in the direction of peak emission translate well for the spectra in the 90 deg direction plotted in Fig. 9. The spectra have somewhat pronounced wiggles at low frequency, suggesting weak reflections, but this is a common occurrence in such measurements (e.g., [10]). Small spectral bumps around $Sr = 3$ are probably due to vortex shedding from the blunt lip of the inner nozzle; they do not affect the general conclusions of this study. The aforementioned trends in OASPL and spectra agree with those of Zaman and Dahl [10] in coaxial jets with similar Mach numbers.

B. Source Localization

We now discuss results arising from the beamforming procedure of Sec. II.B. Figure 10 presents isocontours of $\Phi_{\mathrm{SPL}}(x, Sr)$ for $\theta_{\mathrm{wa}} = 30°$ and for six of the velocity ratios investigated. For the single jet ($U_s/U_p = 0$), the maximum level is located at $x/D = 7.5$ and $Sr = 0.2$. We observe a high-frequency spike as $x \to 0$, indicating that the near-field region emits strong high-frequency noise. Introduction of a slower secondary flow reduces the spike and for $0.356 \leq U_s/U_p \leq 0.694$ the spike disappears. It reappears when the velocity ratio becomes large and the secondary (outer) shear layer now becomes a dominant noise source. The elimination of the high-frequency spike indicates that the secondary flow suppresses near-field noise. The other important trend in Fig. 10 is that with increasing velocity ratio, the peak noise level moves downstream, reflecting the elongation of the primary potential core with addition of the secondary flow. For $U_s/U_p = 1.00$, where the jet essentially becomes a single jet issuing from a larger nozzle, we recover the acoustics of the single ($R000$) jet. The contours for $U_s/U_p = 1.00$ would match closely those for $U_s/U_p = 0.00$ if the axial distance and frequency were nondimensionalized with D_{eff} instead of D_p.

The noise source maps in the direction $\theta_{\mathrm{wa}} = 99°$, shown in Fig. 11, look significantly different from those at $\theta_{\mathrm{wa}} = 30°$ owing to the flatter spectrum in this direction. However, the trends with velocity ratio are fundamentally the same as for $\theta_{\mathrm{wa}} = 30°$: the secondary flow suppresses high-frequency noise near the nozzle exit and extends downstream the location of peak noise. A clearer picture of the effect of the secondary flow on the noise source distribution is gained by computing a differential noise map: that is, the difference

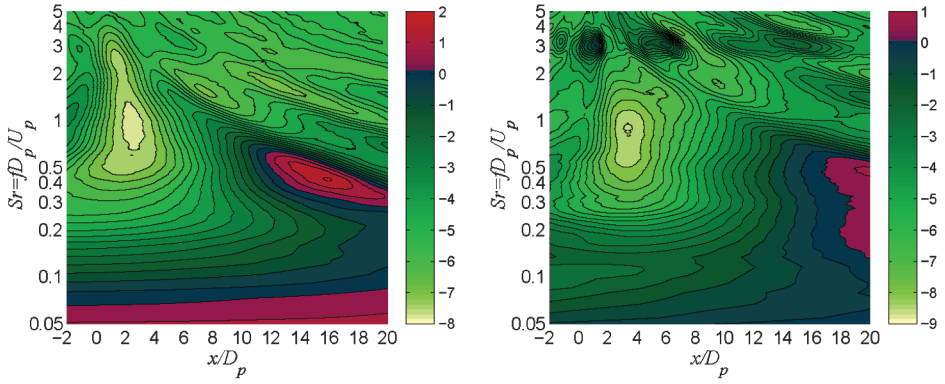

a) **b)**

Fig. 12 Differential noise source maps showing the difference between $U_s/U_p = 0.356$ and 0: a) $\theta_{\mathrm{wa}} = 30°$ and b) $\theta_{\mathrm{wa}} = 99°$.

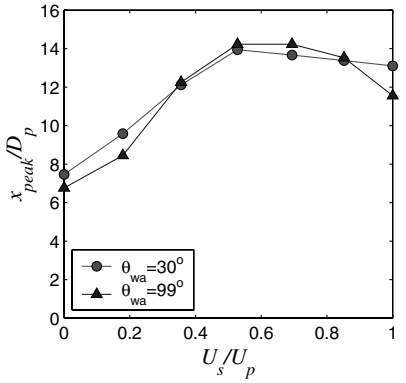

Fig. 13 Axial location of peak noise.

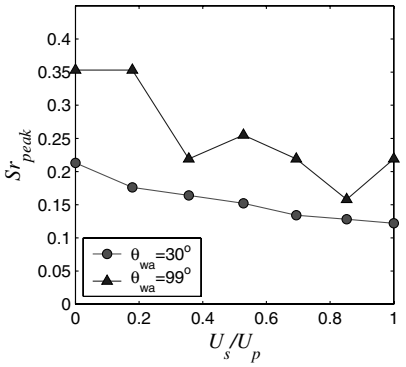

Fig. 14 Strouhal number of peak noise.

between a given configuration and the single jet. The differential maps for $U_s/U_p = 0.356$ are shown in Fig. 12 for array angles $\theta_{\text{wa}} = 30$ and 99°. Green-based colors indicate noise suppression and red-based colors indicate noise increase. In the first two–three jet diameters, the noise sources are suppressed by about 9 dB. There is a moderate increase in low-frequency sound at $x/D \sim 15$, about 2 dB, reflecting the elongation of the high-speed region of the jet. The downstream noise increase is more pronounced at $\theta_{\text{wa}} = 30°$ than at $\theta_{\text{wa}} = 99°$.

The effect of velocity ratio on the space-frequency location of the global peak of the noise source distribution is shown in Fig. 13. The

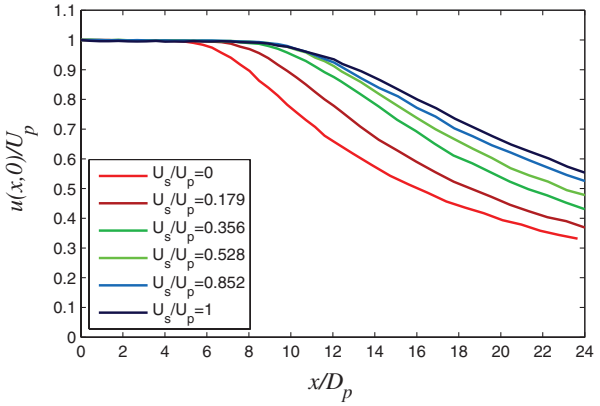

a)

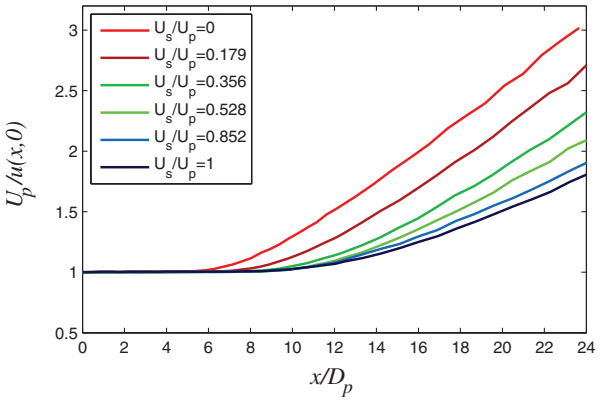

b)

Fig. 16 Axial distribution of a) centerline mean velocity and b) its reciprocal.

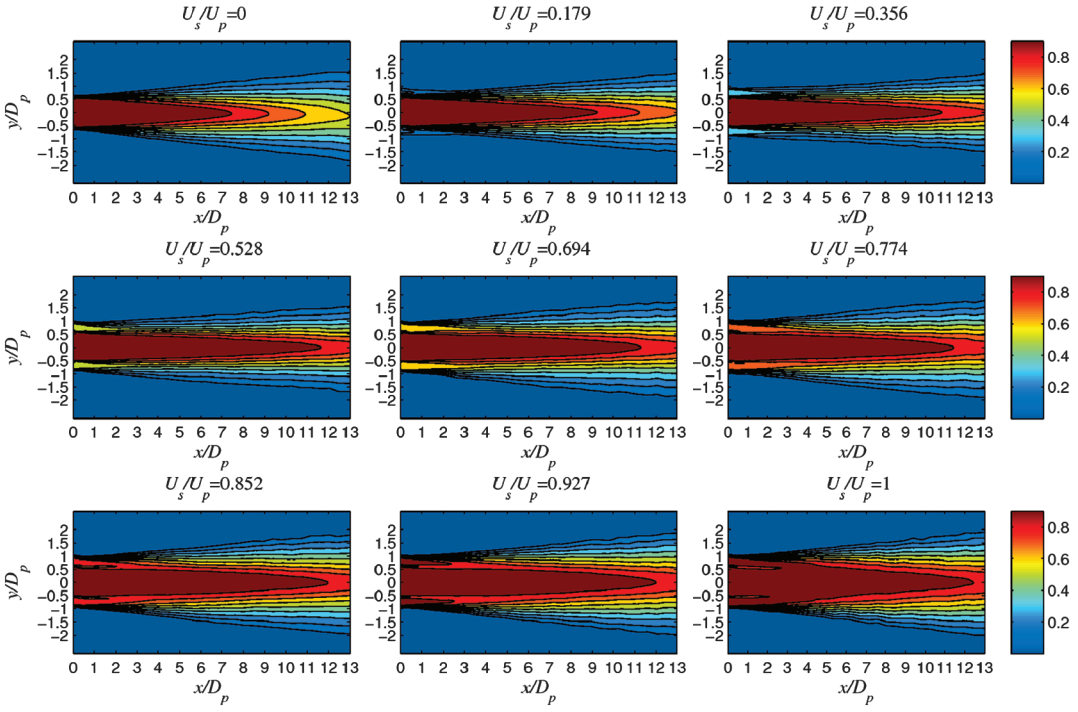

Fig. 15 Contours of $u(x,y)/U_p$.

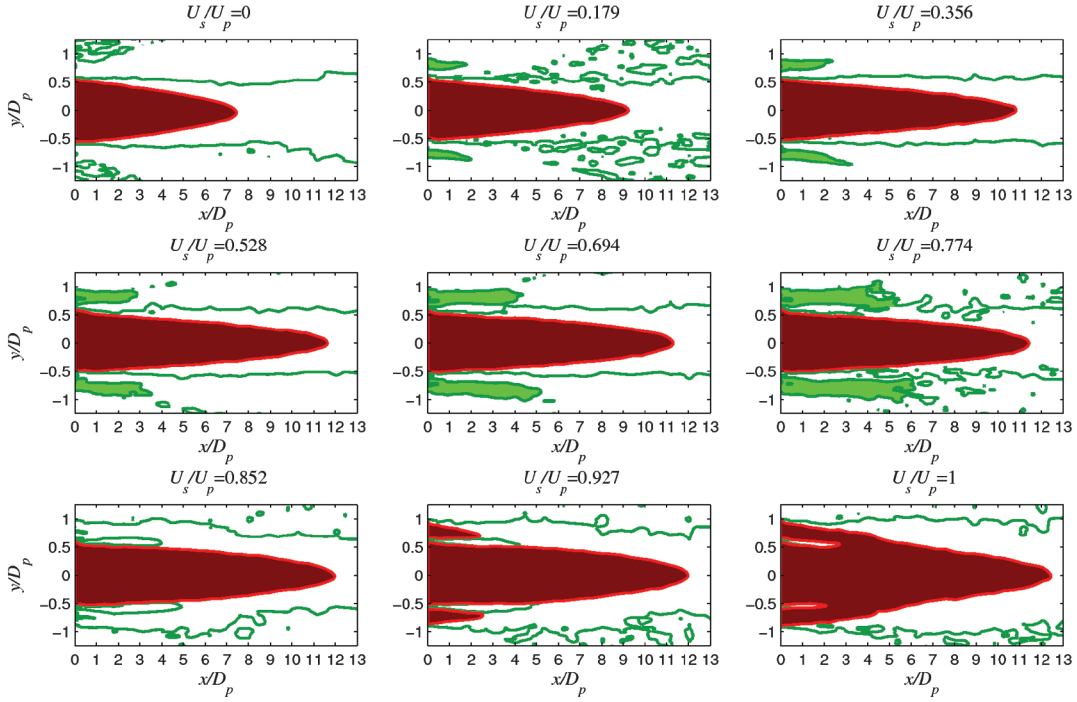

Fig. 17 Locus of inflection points and high-speed region.

axial location of the peak versus velocity ratio follows similar trends for the two array observation angles. It initially increases rapidly with velocity ratio, then reaches a plateau followed by a slight decline. Looking at the average values of the two distributions, the axial location of peak noise moves from $x/D_p = 7.5$ at $U_s/U_p = 0$ to $x/D_p = 13$ at $U_s/U_p = 1$. The Strouhal number of the peak noise, Sr_{peak} decreases with increasing velocity ratio, as shown in Fig. 14. For $\theta_{\text{wa}} = 30°$, Sr_{peak} declines from 0.21 at $U_s/U_p = 0$ to 0.12 at $U_s/U_p = 1$. The corresponding decline for $\theta_{\text{wa}} = 99°$ is 0.40 to 0.22. At $U_s/U_p = 1$ the Strouhal numbers based on D_{eff} are $fD_{\text{eff}}/U_p = 0.20$ and 0.37 for $\theta_{\text{wa}} = 30$ and 99°, respectively, thus coming close to the values of the single jet.

C. Mean Flow

Figure 15 presents isocontours of the mean velocity, normalized by the primary exit velocity, on the x-y plane for all the velocity ratios investigated. For clarity, the figure covers only the near-field region $0 \le x/D_p \le 13$. Using the threshold $u/Up \ge 0.9$ to define the primary core of the jet (Fig. 1), we observe a substantial elongation of the primary core with velocity ratio. The primary core length x_p increases from $x_p/D_p = 8.0$ at $U_s/U_p = 0$ to $x_p/D_p = 13.0$ at $U_s/U_p = 1$. This increase by factor of 1.62 is consistent with the diameter ratio $D_{\text{eff}}/D_p = 1.57$. We also note the increased prominence of the secondary core as the velocity ratio increases, up to the value $U_s/U_p = 0.774$. Above this value, the velocity difference between the primary and secondary streams becomes very small and the secondary core is not as discernible. In addition, we observe the emergence of the wake region from the lip of the primary nozzle at velocity ratios close to 1.0. The axial distribution of centerline velocity is plotted in Fig. 16a for several velocity ratios. The flat part of each curve corresponds to the potential core region. The figure indicates that a small increase of the velocity ratio from zero results in a significant elongation of the potential core. However, the trend saturates with increasing velocity ratio. The inverse of the centerline velocity, plotted in Fig. 16b, illustrates that the decay rate decreases as U_s/U_p increases.

Computation of the second y derivative of the mean velocity enables location of the inflectional regions of the jet ($\partial^2 u/\partial y^2 = 0$). The loci of the inflection points on the x-y plane are shown as green lines in Fig. 17 for all the velocity ratios investigated. Each figures includes the extent of the primary core, defined by the $u/U_p > 0.9$ criterion. The inflectional layers ($i_2 - i_3$ loop in Fig. 1) are highlighted for clarity. The figures include some extraneous small islands of inflection points that are the result of noise in the velocity profiles. They can be removed by increasing the filter size used to compute the derivatives; however, this comes at the risk of under-resolving the inflectional layers. The plots indicate a significant elongation of the secondary core, defined by the $i_2 - i_3$ loop, with increasing velocity ratio. For $U_s/U_p > 0.774$, we cannot resolve inflectional layers for two reasons: the velocity difference between primary and secondary streams becomes too small, and the wake effect creates its own inflection points and thus prevents clear identification of the i_2 and i_3 points.

The mean flow trends are summarized in Fig. 18, in which we plot the length of the primary and secondary cores versus velocity ratio. As inferred from Fig. 16, the primary core shows a fast initial rise followed by slower growth at high velocity ratio. The slow-growth part contains a peculiar plateau near $U_s/U_p = 0.6$ which is not presently understood. The secondary core grows in a somewhat linear fashion with U_s/U_p, reaching a length $x_s/D_p = 6$ at $U_s/U_p = 0.774$. The behavior of x_s beyond this point is not clear, except that it has to be zero at $U_s/U_p = 1$. Ideally, if there were no wake effect, we expect that it should be measurable up to velocity ratios just below 1.0 and that it would continue to increase up to that point.

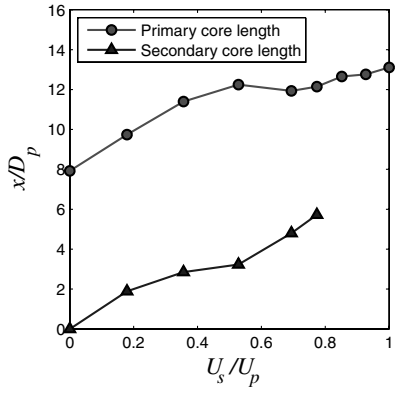

Fig. 18 Primary and secondary core lengths versus velocity ratio.

We now make some connections between the mean flow trends and the phased array results. Comparing Figs. 13 and 18, we observe a strong similarity between the location of peak noise and the end of the primary core. It is thus evident that the strongest noise comes from the end of the primary core and that the extension of the primary core leads to an elongation of the noise source region. With regards to the secondary core trends of Fig. 18, we note that for $U_s/U_p = 0.354$ $x_s/D_p = 3$. This length is sufficient to cover the region of high-frequency noise generation of the single jet, evident in the plots of Figs. 10 and 11. This explains the suppression of high-frequency noise by the secondary flow. The effect of the secondary core is even more evident in the differential noise source maps of Fig. 12, in which the axial location of maximum reduction, $x/D_p = 3$, coincides with the measured length of the secondary core. This silencing effect of the secondary core is observed for $0.18 < U_s/U_p < 0.85$.

IV. Conclusions

The noise source distribution of coaxial jets with a diameter ratio of 1.6 and variable velocity ratio was investigated with a narrow-aperture microphone phased array. The array design enabled discrimination between noise emitted by large-scale turbulence (direction of peak emission, $20° < \theta < 30°$) and noise emitted by fine-scale turbulence (broadside and forward directions, $\theta > 70°$). The acoustic data were complemented with surveys of the mean velocity, which enabled measurement of the primary and secondary cores of the jet. For zero velocity ratio (single-stream jet), the region near the nozzle emits strong high-frequency noise. Increasing the velocity ratio suppresses this noise by as much as 9 dB and extends downstream the location of the peak noise, which increases moderately. The location of peak noise tracks well the end of the primary core. The suppression of high-frequency noise is explained by the creation and elongation of the secondary core as the velocity ratio increases. The near-nozzle noise reduction is consistent with the reduced shear and reduced convective Mach number elucidated in earlier studies [12,13]. The acoustic trends with velocity ratio are similar for the two array observation angles (30 and 99°) from which large-scale and fine-scale turbulence noise, respectively, have been shown to radiate. However, the increase in peak noise is more pronounced for the large-scale noise. The results indicate that the coaxial jet has a noise source distribution fundamentally different from that of a single-stream jet.

References

[1] Forstall, W., Jr., and Shapiro, A. H., "Momentum and Mass Transfer in Coaxial Gas Jets," *Journal of Applied Mechanics*, Vol. 17, No. 4, 1950, pp. 399–408.

[2] Ko, N. W. M., and Kwan, A. S. H., "The Initial Region of Subsonic Coaxial jets," *Journal of Fluid Mechanics*, Vol. 73, Part 2, 1976, pp. 305–332.

[3] Champagne, F. H., and Wygnanski, I. J., "An Experimental Investigation of Coaxial Turbulent Jets," *International Journal of Heat and Mass Transfer*, Vol. 14, No. 9, 1971, pp. 1445–1464. doi:10.1016/0017-9310(71)90191-8

[4] Durao, D., and Whitelaw, J. H., "Turbulent Mixing in the Developing Region of Coaxial Jets," *Journal of Fluids Engineering*, Vol. 95, No. 3, 1973, pp. 467–473.

[5] Williams, T. J., Ali, M. R. M. H., and Anderson, J. S., "Noise and Flow Characteristics of Coaxial Jets," *Journal of Mechanical Engineering Science*, Vol. 11, No. 2, 1969, pp. 133–142. doi:10.1243/JMES_JOUR_1969_011_017_02

[6] Murakami, E., and Papamoschou, D., "Mean Flow Development in Dual-Stream Compressible Jets," *AIAA Journal*, Vol. 40, No. 6, 2002, pp. 1131–1138. doi:10.2514/2.1762

[7] Bogey, C., Barre, S., Juve, D., and Bailly, C., "Simulation of a Hot Coaxial Jet: Direct Noise Prediction and Flow-Acoustics Correlations," *Physics of Fluids*, Vol. 21, No. 3, 2009, Paper 035105. doi:10.1063/1.3081561

[8] Tanna, H. K., "Coannular Jets—Are They Really Quiet and Why?," *Journal of Sound and Vibration*, Vol. 72, No. 1, 1980, pp. 97–118. doi:10.1016/0022-460X(80)90710-5

[9] Tanna, H. K., and Morris, P. J., "The Noise from Normal-Velocity-Profile Coannular Jets," *Journal of Sound and Vibration*, Vol. 98, No. 2, 1985, pp. 213–234. doi:10.1016/0022-460X(85)90386-4

[10] Zaman, K. B. M. Q., and Dahl, M. D., "Noise and Spreading of a Subsonic Coannular Jet—Comparison with Single Equivalent Jet," *AIAA Journal*, Vol. 45, No. 11, 2007, pp. 2661–2670. doi:10.2514/1.29441

[11] Papamoschou, D., "Engine Cycle and Exhaust Configurations for Quiet Supersonic Propulsion," *Journal of Propulsion and Power*, Vol. 20, No. 2, 2004, pp. 255–262. doi:10.2514/1.9251

[12] Fisher, M. J., Preston, G. A., and Bryce, W. D. "A Modelling of the Noise from Simple Coaxial Jets, Part 1: With Unheated Primary Flow," *Journal of Sound and Vibration*, Vol. 209, No. 3, 1998, pp. 385–403. doi:10.1006/jsvi.1997.1218

[13] Papamoschou, D., "New Method for Jet Noise Suppression in Turbofan Engines," *AIAA Journal*, Vol. 42, No. 11, 2004, pp. 2245–2253. doi:10.2514/1.4788

[14] Henderson, B., Norum, T., and Bridges, J., "An MDOE Assessment of Nozzle Vanes for High Bypass Ratio Jet Noise Reduction," AIAA Paper 2006-2543, May 2006.

[15] Zaman, K. B. M. Q., and Papamoschou, D., "Effect of a Wedge on Coannular Jet Noise," AIAA Paper 2006-0007, Jan. 2006.

[16] DeBonis, J. R., "RANS Analyses of Turbofan Nozzles With Internal Wedge Deflectors for Noise Reduction," *Journal of Fluids Engineering*, Vol. 131, No. 4, 2009, Paper 041104. doi:10.1115/1.3089536

[17] Dippold, V., Foster, L., and Wiese, M., "Computational Analyses of Offset-Stream Nozzles for Noise Reduction," *Journal of Propulsion and Power*, Vol. 25, No. 1, 2009, pp. 204–217. doi:10.2514/1.34943

[18] Billingsley, J., and Kinns, R., "The Acoustic Telescope," *Journal of Sound and Vibration*, Vol. 48, No. 4, 1976, pp. 485–510. doi:10.1016/0022-460X(76)90552-6

[19] Humphreys, W. M., Brooks, T. F., Hunter, W. W., and Meadows, K. R., "Design and Use of Microphone Directional Arrays for Aeroacoustic Measurements," AIAA Paper 98-0471, Jan. 1998.

[20] Narayanan, S., Barber, T. J., and Polak, D. R., "High Subsonic Jet Experiments: Turbulence and Noise Generation Studies," *AIAA Journal*, Vol. 40, No. 3, 2002, pp. 430–437. doi:10.2514/2.1692

[21] Lee, S. S., and Bridges, J., "Phased-Array Measurements of Single Flow Hot Jets," AIAA Paper 2005-2842, May 2005.

[22] Papamoschou, D., and Dadvar, A., "Localization of Multiple Types of Jet Noise Sources," AIAA Paper 2006-2644, May 2006.

[23] Strange, P. J. R., Podmore, G., Fisher, M. J., and Tester, B. J., "Coaxial Jet Noise Source Distributions," AIAA Paper 1984-2361, Oct. 1984.

[24] Battaner-Moro, J. P., "New Automated Source Breakdown Algorithm for Jet Noise," AIAA Paper 2003-3324, May 2003.

[25] Bridges, J., "Effect of Heat on Space-Time Correlations in Jets," AIAA Paper 2006-2534, May 2006.

[26] Papamoschou, D., and Debiasi, M., "Directional Suppression of Noise from a High-Speed Jet," *AIAA Journal*, Vol. 39, No. 3, 2001, pp. 380–387. doi:10.2514/2.1345

[27] Tam, C. K. W., Golebiowski, M., and Seiner, J. M., "On the Two Components of Turbulent Mixing Noise from Supersonic Jets," AIAA Paper 96-1716, May 1996.

[28] Tinney, C. E., and Jordan, P., "The Near Pressure Field of Co-Axial Subsonic Jets," *Journal of Fluid Mechanics*, Vol. 611, 2008, pp. 175–204.

[29] Bass, H. E., Sutherland, L. C., Blackstock, D. T., and Hester, D. M., "Atmospheric Absorption of Sound: Further Developments," *Journal of the Acoustical Society of America*, Vol. 97, No. 1, 1995, pp. 680–683. doi:10.1121/1.412989

[30] Savitzky, A., and Golay, M. J. E., "Smoothing and Differentiation of Data by Simplified Least Squares Procedures," *Analytical Chemistry*, Vol. 36, No. 8, 1964, pp. 1627–1639. doi:10.1021/ac60214a047

A. Lyrintzis
Associate Editor